Nanoscale

PAPER

View Article Online
View Journal | View Issue

Cite this: *Nanoscale*, 2018, **10**, 3953

Mechanochromic MOF nanoplates: spatial molecular isolation of light-emitting guests in a sodalite framework structure†

Abhijeet K. Chaudhari and Jin-Chong Tan *

Mechanochromic materials have a wide range of promising technological applications, such as photonics-based sensors and smart optoelectronics. The examples of mechanochromic metal–organic framework (MOF) materials, however, are still relatively uncommon in the literature. Herein, we present a previously undescribed Guest@MOF system, comprising "Perylene@ZIF-8" nanoplates, which will undergo a reversible 442 nm ⇌ 502 nm photoemission switching when subjected to a moderate level of mechanically-induced pressure at several tens of MPa. The nanoplates were constructed *via* high-concentration reaction (HCR) strategy at ambient conditions to yield a crystalline ZIF-8 framework hosting the luminous Perylene guests. The latter confined within the porous sodalite cages of ZIF-8. Remarkably, we show that in a solid-state condition, it is the spatial isolation and nano-partitioning of the luminescent guests that bestow the unique solution-like optical properties measured in the host–guest assembly. As such, we demonstrate that switchable red- or blue-shifts of the visible emission can be accomplished by mechanically modifying the nanoscale packing of the nanoplates (*e.g.* monoliths, pellets). Theoretical calculations suggest that the elasticity of the host's sodalite cage coupled with the intermolecular weak interactions of the confined guest are responsible for the unique mechanochromic luminescence behavior observed.

Received 31st December 2017,
Accepted 18th January 2018

DOI: 10.1039/c7nr09730a

rsc.li/nanoscale

1. Introduction

Functional nanomaterials with adjustable luminescence properties[1–3] are greatly sought after to achieve new generation photonics-based sensing and tunable optoelectronics applications.[4–6] Indeed, a vast range of fluorescent materials, including conjugated organic molecules, metal complexes, liquid crystals, oligomers, polymers, metallogels, supramolecular assemblies, and quantum dots have shown huge potential for use in numerous luminescence-based devices and sensors.[7–10] One of the intriguing findings in this topic is mechanochromic luminescence. A mechanochromic material switches emission when subjected to a mechanical force (stress).[11] They have gained increasing attention in the recent years. Researchers seek to understand, control, and tune the luminescence properties with the help of exogenous mechanical stimuli, such as shearing, grinding, and rubbing, tension, compression, torsion, and impact. It is envisaged that smart mechanochromic materials can be integrated into deformation-based detectors, security papers, optical memories, and photonic strain gauges.[12,13] Regarding material design, it is essential to control its intermolecular weak interactions, which are dictating the optical behavior as a function of mechanical stress and strain.[14,15] Outstanding challenges in the field including the aggregation-caused quenching (ACQ), solid-state phase change, and amorphization present limited structural resilience and difficulty in the precise control of molecular orientations needed for the practical applications. Traditional approaches for preparing mechanochromic materials often require complicated molecular designs and will involve difficult multistep synthetic procedures.[16–19] To address the foregoing challenges, one possible solution is to combine chemical traits of existing fluorophoric molecules into the ordered nanoscale host assemblies by leveraging the host–guest spatial confinement strategy.[20–23]

Metal–organic frameworks (MOFs)[24,25] have been intensely studied for over two decades for their high porosity and long-range crystalline network, combined with designable chemical environments and tunable physical properties.[26–29] To trigger the switchable optical properties of the guest molecules under the confinement of the nanoscale pores in the MOF host, the dynamic MOF systems are highly desirable owing to their

Multifunctional Materials & Composites (MMC) Laboratory, Department of Engineering Science, University of Oxford, OX1 3PJ Oxford, UK.
E-mail: jin-chong.tan@eng.ox.ac.uk

†Electronic supplementary information (ESI) available: Detailed synthesis procedures; microstructural characterization by TEM and AFM; TGA data; photoluminescence spectra of pellets pressed at different pressures; band gap calculations; XRD structural refinement results. See DOI: 10.1039/C7NR09730A

structural versatility. Recently, we shed light on the dynamics of zeolitic imidazolate frameworks (ZIFs, a topical class of MOFs)[30] *via* terahertz vibrational spectroscopy[31] and demonstrated the efficacy of the sodalite cage of ZIF-8 for hosting the bulky metal complexes to engineer a luminescent material with an improved photostability.[22] In this study, we combined our understanding of the dynamic behavior of the ZIF-8 framework and its use as a host for accommodating the external guest species to contrive a new mechanochromic host–guest material. There are already a few examples of the (host-only) mechanochromic MOFs reported in the literature (*e.g.* in ref. 32–36), in which the mechanochromism originated typically from the N-donor-based coordinating linkers. To the best of our knowledge, the host–guest system reported herein is the first example of a mechanochromic material, demonstrating the spatially ordered fluorophoric guests constrained in a periodic MOF structure.

2. Results and discussion

2.1. Guest@MOF encapsulation achieved by high concentration reaction

A facile reaction of 2-methylimidazole (mIm) with Zn(II) cations yields the formation of ZIF-8, adopting the sodalite framework topology.[37] ZIF-8 is a highly topical MOF structure for encapsulation of the functional guest molecules (for example see ref. 22 and 38–45) because it features long-range periodicity with a relatively large pore (about 1 nm diameter) located in the center of each sodalite cage. The ease of synthesis combined with the unique porous architecture and mechanical properties of ZIF-8 (elasticity[46] and dynamics)[31] could offer vast possibilities to engineer the novel Guest@MOF systems exhibiting tunable functionalities.

In this study, we exploited the spherical voids of ZIF-8 as the spatially arranged "host" spaces, allowing the encapsulation of the polycyclic aromatic hydrocarbon, Perylene ($C_{20}H_{12}$), which is an efficient light-emitting "guest" molecule. We adopted the concept of high-concentration reaction (HCR), introduced recently by our group,[21,47] to synthesize a new host–guest assembly termed "Perylene@ZIF-8" at the ambient conditions. The detailed synthetic procedures are described in the ESI.† In essence, the proposed self-assembly route enables us to achieve nanoscale spatial confinement of the bulky Perylene guest molecules in the voids of the ZIF-8 host. The introduction of triethylamine (NEt_3) during HCR not only accelerates the reaction process, resulting in a high amount of Perylene@ZIF-8 product (see Fig. S1 in ESI†), but also provides an additional control over the morphology of the product, specifically the downsizing of the 3-D framework architecture of the ZIF-8 material to derive two-dimensional (2-D) nanoplates (Fig. 1).

Fig. 1 shows the 2-D morphologies of the Perylene@ZIF-8 compound obtained in our study. Transmission electron microscopy (TEM) and atomic force microscopy (AFM) were applied to characterize the microstructural features of the

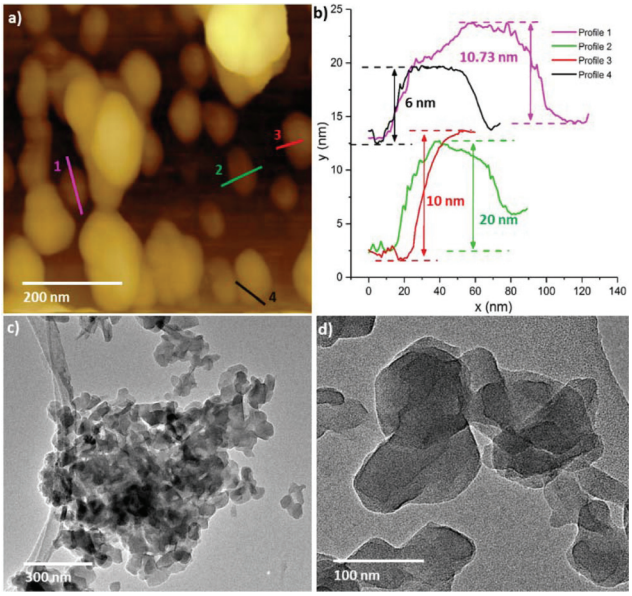

Fig. 1 (a) AFM topography image of nanoplates of Perylene@ZIF-8. (b) Representative thickness profiles of nanoplates obtained from the AFM image in (a), indicating a typical thickness of the order of tens of nm. (c) TEM micrograph showing the aggregated nature of the finer scale Perylene@ZIF-8 nanoplates. (d) A higher-magnification TEM image showing the intertwined 2-D microstructural features of the nanoplates.

nanoplates. We found that the lateral size of the nanoplates of Perylene@ZIF-8 varies from about 15 nm to 150 nm. However, their thickness ranges from 6 nm to 20 nm (Fig. 1a and b). The TEM micrographs (Fig. 1c and d) reveal that indeed the HCR product consists of an aggregation of intertwining finer scale nanoplates (see additional micrographs in Fig. S2–S4 in the ESI†). Notably, the aggregated nanoplates will readily transform into a monolith simply by drying at 90 °C under vacuum for 6 h (Fig. S1†), which can be attributed to the densification of the intertwined 2-D nanoplates.

Interestingly, we discovered that the optical properties of the monolithic form of Perylene@ZIF-8 and its fine powder counterpart (*viz.* ground monolith) are distinctively different as summarised in Fig. 2. It can be observed that the monolith material emits a light yellow-green emission when excited under a 365 nm UV light (Fig. 2a and b). However, grinding of the monolith into a fine powder resulted in a blue shift in the emission at the lower wavelength. This drastic change in emission behavior due to the mechanical grinding effect has inspired us to investigate the phenomenon in detail. We found that, as depicted in Fig. 2c, the peaks of the fine powders experience a red-shift (442 nm → 502 nm) when being mechanically compressed into a pellet utilizing a relatively low pressure of less than about 40 MPa. Conversely, we show that by breaking the pellet down into a fine powder, a blue-shift (502 nm → 442 nm) is produced instead, as illustrated in Fig. 2d. This effect is reversible upon the application and the removal of mechanical forces. In the subsequent sections, we shall discuss the mechanochromic luminescence mechanism

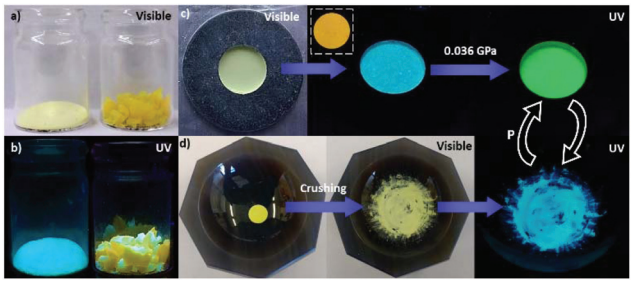

Fig. 2 (a) Fine powder and monolithic form of Perylene@ZIF-8 seen in the visible light and (b) their distinctively different emissions observed under the 365 nm UV excitation. (c) Reversible mechanochromic luminescent behavior (442 ⇌ 502 nm) of Perylene@ZIF-8: a pale-yellow powder (hand pressed into a metallic mold ∅ 13 mm) seen under visible light and under 365 nm UV excitation, a red-shift in emission to green 502 nm can be seen upon the application of 0.036 GPa pressure. Inset shows the deep-orange emission of a pristine Perylene pellet under UV for comparison. (d) A dark-yellow pellet observed under visible light, showing the recovery of the light-blue 442 nm emission (under UV) after being crushed to recover a fine powder form.

underpinning Perylene@ZIF-8 using UV-Vis spectroscopy, theoretical band gap calculations, and X-ray diffraction techniques.

2.2. Photophysical characterization to reveal host–guest interactions and energy transfer

We performed diffuse reflectance spectroscopy to correlate the mechanochromic behavior to the salient changes in the molecular structure of the host–guest assembly. Fig. 3a shows a broad absorption peak detected between 255 and 510 nm for the Perylene@ZIF-8 monolith, which is completely absent in the pristine ZIF-8. This result confirms the successful confinement of Perylene (guest) within the spherical voids of ZIF-8 (host). In particular, the spectra show significant changes in the absorption properties of Perylene@ZIF-8 when it was converted from a monolith into a powder form (by grinding in a mortar). More precisely, the distinct absorption band at 304 nm experienced a sharp decline in its intensity when the monolith was crushed into the powder form. This finding indi-

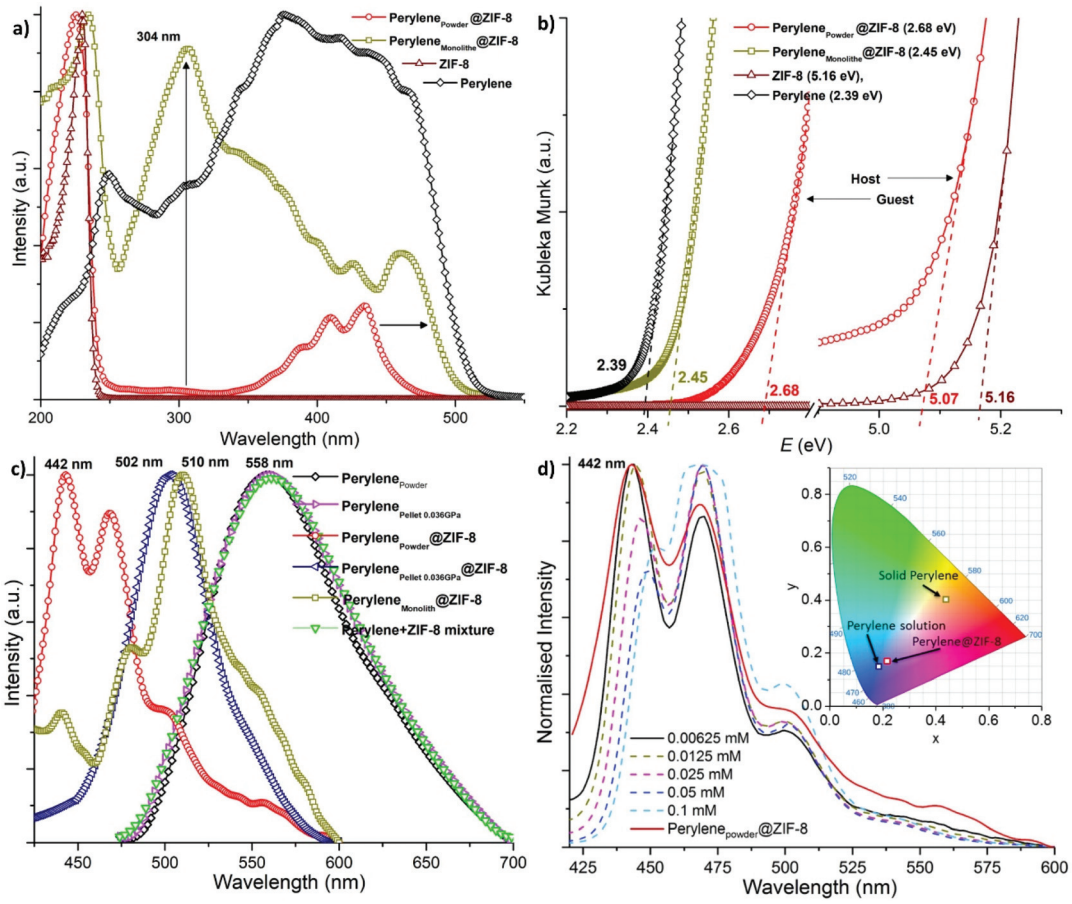

Fig. 3 (a) Comparison of absorption behavior obtained from diffuse reflectance of the pristine host (ZIF-8), pristine guest (solid Perylene), and host–guest system (Perylene@ZIF-8). (b) Kubelka–Munk (KM) function for determining the band gaps based on the photon energy intercepts. (c) Fluorescence emission spectra of the pristine Perylene powder compared with Perylene@ZIF-8, Perylene pellet, and physically mixed Perylene + ZIF-8 compounds when excited at 365 nm. (d) Emission spectra of different concentrations of Perylene solution (in dichloromethane) and solid-state Perylene$_{powder}$@ZIF-8. Inset: CIE 1931 colour chromaticity diagram showing the drastic effect of Perylene confinement within ZIF-8 in the solid state and how this behavior resembles the dilution of the Perylene solution at a very low concentration of 0.00625 mM.

cates that the monolith has a pronounced π–π* transition because of the densely-packed arrangement of the nanoplate aggregates, which disappears after being converted into the loosely-packed powder form. This notion is further supported by the following observations. (i) The disappearance of the broad absorption band associated with the Perylene guest species, which transforms into the multiple more well-defined peaks between 380 and 450 nm when the monolith is crushed into powder. (ii) The absorption peak observed at 225 nm corresponding to the pristine ZIF-8 structure blue-shifted by about 10 nm when the monolith is converted into the powders, again signifying a decline in its nominal packing density.

Unlike the absorption spectra of pure Perylene in the solid state, we note that spatially confined Perylene has absorption bands akin to the bands observed in the liquid solution.[48] Allendorf *et al.*[49] described the "solution-like" optical properties in the case of the organic linkers in the solid state as a result of spatial isolation due to the MOF formation. The similar effects are observed in the current host–guest system, but the difference here is that the guest molecules (not linkers) have been spatially isolated through the 3-D partitioning afforded by the MOF porosity. The weak intermolecular interactions, such as the π–π interactions, could modify the optical behavior. Being structurally planar and aromatic in nature, the Perylene molecule may readily establish π–π stacking. Therefore, a deep-orange emission is observed for the solid Perylene powder (Fig. 2c inset). The similar effects have been reported in the organic molecules due to the formation of the J (or H) type of aggregates.[50] In particular, the ZIF-8 host environment offers to tune the weak interactions of the confined Perylene guest emitters. In our previous report, we mentioned the ability of ZIF-8 for making the weak interactions *via* the 2-methylimidazole (mIm) linkers.[22] Similarly, in this case, the confined Perylene molecules could establish CH–π and/or π–π interactions with the adjacent imidazole rings. In fact, the resultant broad emission band of the monolith from 430 nm to 600 nm (Fig. 3c) can be explained by the presence of the weak host–guest interactions elucidated above.

Direct evidence of the intermolecular weak interactions was witnessed from the modifications to the band gap values, determined from the diffuse reflectance data. Fig. 3b shows the increase in band gap of Perylene@ZIF-8when converted from monolith (2.45 eV) to fine powder (2.68 eV). The electronic properties of the host framework (ZIF-8) are found to be affected by the guest confinement with its band gap decreasing from 5.16 eV to 5.07 eV. Conversely, the band gap of the Perylene guest molecule increased due to spatial confinement compared to that of pure Perylene solid.

Fig. 4 presents the theoretical band gap calculations confirming this outcome. The calculated band gap of Perylene was found to rise from 1.313 eV to 1.793 eV when it is positioned in a confined pore environment. However, the calculated band gap of the distorted ZIF-8 host (see section 2.3 for details about the distorted ZIF-8 structure) was found to be relatively lower (4.361 eV) as compared to that of a cubic ZIF-8 structure

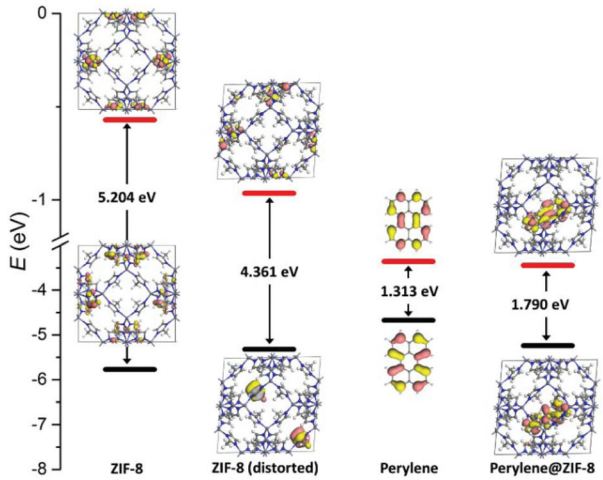

Fig. 4 Effect of the host–guest confinement on the band gap of Perylene was calculated theoretically, which followed the trends observed experimentally in Fig. 3. Symbols used: HOMO (black) – LUMO (red) for the energy levels; dark pink and yellow iso-surfaces representing the positive and negative charges of the molecular orbitals.

(5.204 eV). A good qualitative agreement in terms of the band gap values can be observed between the experiments and theoretical trends associated with the host–guest confinement effects. These new results illustrate the potential of accomplishing band gap engineering by exploiting the Guest@MOF confinement strategy.

From the photograph of the monoliths shown in Fig. 2b, interestingly, we may observe that there are different regions displaying light-green to dark-yellow emissions when they are subjected to the UV excitation. The edges of the monolith primarily emit a lighter green-blue color, which can be assigned to the emission of the 'loosely packed' nanoplates of Perylene@ZIF-8, while a darker yellow-green emission can be assigned to the regions containing the 'densely packed' nanoplates. These varying color characteristics are detectable in the emission spectrum of the monolith shown in Fig. 3c, which displays the spectral hump and shoulder located at 440 nm and 479 nm, respectively. We reasoned that additional small humps observed at, for instance, 543, 554, 568, and 581 nm, could arise due to the entrapped Perylene molecules between the aggregations of 2-D nanoplates (but not within the ZIF-8 pores). Surprisingly, the maximum emission observed at 510 nm in the case of monolithic Perylene@ZIF-8 could not be attained by the reconstituted fine powders (mechanically compressed into a pellet). Instead, an emission spectrum with only a single feature, λ_{max} = 502 nm, is observed for the pellet of Perylene@ZIF-8 pressed under 0.036 GPa. Similar to the absorption, the fluorescence of the finely ground powder obtained from the monolithic Perylene@ZIF-8 also shows a solution-like emission behavior. Indeed, we confirmed this phenomenon by the results presented in Fig. 3d. The emission spectra of the Perylene solutions with different concentrations in dichloromethane reveal that the aggregation of molecules in a solution state causes the merging of the peaks at around

450 nm, but upon dilution, the merged peaks become increasingly separated to eventually give a maximum emission at 442 nm. This is in good agreement with the solid-state spectra of $Perylene_{powder}$@ZIF-8. In particular, the heavily diluted Perylene with a concentration of 0.00625 mM shows less influence from its neighboring molecules, which is precisely the "solution-like" effect observed in the solid-state when the Perylene molecules were spatially separated through nanoconfinement within the ZIF-8 host framework. Fig. 3d clearly shows the transition of emission behavior of the concentrated and diluted solutions and how it finally overlaps (at 442 nm) with the solid-state emission spectrum of $Perylene_{powder}$@ZIF-8.

As shown in Fig. 3c, the emission of the reconstituted pellet at 502 nm suggests that the dense packing achieved in the original monolith (obtained from drying a wet sample post-synthesis) cannot be fully recovered upon the strain relaxation after being ground into the powder form. Therefore, the emission of the monolith observed at a relatively higher wavelength of 510 nm can be attributed to the greater charge transfer between densely aggregated nanoplates. We propose a mechanism behind the mechanochromic response of Perylene@ZIF-8 nanoplates, as illustrated in Fig. 5. It is reasonable to expect some microscopic-sized voids to be present between the randomly-oriented nanoplates in the powdered form (Fig. 5a). After the application of an external pressure during the pelletization process, its packing will improve, thus offering a better inter-nanoplate interaction to enhance the electronic charge delocalization between the adjacent nanoplates (Fig. 5b), facilitated by the electron-rich Perylene guest entrapped in the pores of the sodalite cages of the ZIF-8 host.

The modification of the electronic structure of the host–guest assembly is presented in Fig. 4, calculated using density functional theory (DFT). Theoretical band gap energy levels provide additional insights into the plausible energy transfer pathway from the LUMO (the lowest unoccupied molecular orbital) of ZIF-8 to the LUMO of Perylene upon photoexcitation. The HOMO (the highest unoccupied molecular orbital) of Perylene@ZIF-8 shows an electronic distribution that is highly localized on the Perylene molecules with a limited sharing with the C=C bonds in the imidazole moiety of the ZIF-8 host. The LUMO of Perylene@ZIF-8 is exclusively occupied by the Perylene molecule, indicating the propensity for the energy transfer between the hybrid orbitals of the host–guest assembly and the guest species confined within it. The role of the flexible nature of the ZIF-8 framework can be observed in the reduction of the band gap energy (about 1 eV) upon shear distortion of the host structure,[46] which is again important in the context of the host–guest assembly for establishing the intermolecular interactions upon the application of an external pressure. It is well-documented in the literature that the planarity of the molecules will contribute to the reduction of band gaps by facilitating the conjugation of adjacent molecules.[51] On this basis, we suggest that under pressure or mechanical stress, the elasticity of ZIF-8[46] permits better planarity to be established between the local intermolecular alignment of mIm···Perylene, leading to the "molecular wire effect"[52] (Fig. 5b) that could account for the red shifts we observed in the absorption and emission spectra (Fig. 3).

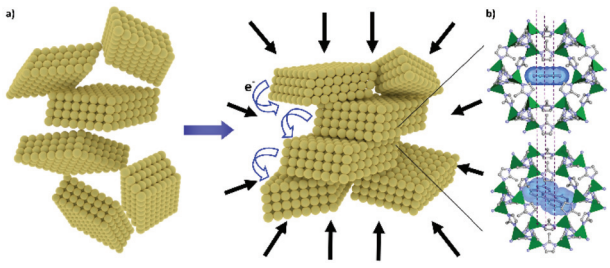

Fig. 5 Schematic diagram representing (a) the randomly oriented nanoplates of Perylene@ZIF-8 with the presence of the air gaps in the powder form due to its loosely-packed configuration. Upon compaction by an externally applied hydrostatic pressure, the nanoplates rearrange themselves to become more densely aggregated together. (b) Proposed energy transfer pathway of two adjacent nanoplates attributed to the "molecular wire effect", facilitated by the π–π interactions connecting the mIm···Perylene···mIm molecular pathways.

2.3. Structural evolution as a function of compressive stress

The X-ray diffraction (XRD) technique was used to characterize the structural changes in the ZIF-8 host. It can be inferred that the XRD pattern of Perylene@ZIF-8 monolith (Fig. 6a) reveals its crystalline nature, but with the presence of relatively broad peaks. The monolith was ground (in a mortar using a pestle) for 5 min to yield a 'powder' sample, with which we detected the sharper Bragg peaks; some of the peaks coincided with the simulated pattern of an ideal ZIF-8 structure. However, in addition to all of the matching primary peaks, the splitting and broadening of the peaks were observed, indicating the reduction in cubic cell symmetry of ZIF-8 due to structural distortion. Hence, we performed Pawley structural refinement on the experimental powder data, establishing the precise changes to the cell parameters of the host. The results shown in Fig. 6b and Table S1 (ESI†) reveal that the nanoplates have a triclinic cell symmetry. It was observed that $a = b = c = 16.992$ Å of cubic ZIF-8 increased to $a = 17.339$ Å, $b = 17.127$ Å, and $c = 17.072$ Å, while $\alpha = \beta = \gamma = 90°$ of its cubic cell deformed to $\alpha = 87.073°$, $\beta = 90.321°$, and $\gamma = 84.677°$ due to structural distortion. The cell expansion of the host framework can be attributed to the spatial confinement of the bulky Perylene guest molecules in the pores of ZIF-8. This is accompanied by the reduction of the α and γ angles, which can be explained by the shear deformation[46] (inset of Fig. 6b) of the 2-D nanoplate morphology from the aggregation-induced mechanical strains.

Subsequently, we ground the above 'powder' sample for another 20 min to achieve a 'fine powder' sample. The XRD pattern of the latter exhibits the broadened Bragg peaks as evidenced in Fig. 6a. The disappearance of the peak splitting can be ascribed to the relaxation of strains in the aggregated nanoplates, while the peak broadening observed is indicative of the formation of finer scale particles by crushing the larger aggregates. To test the effect of grinding on emission, we compared

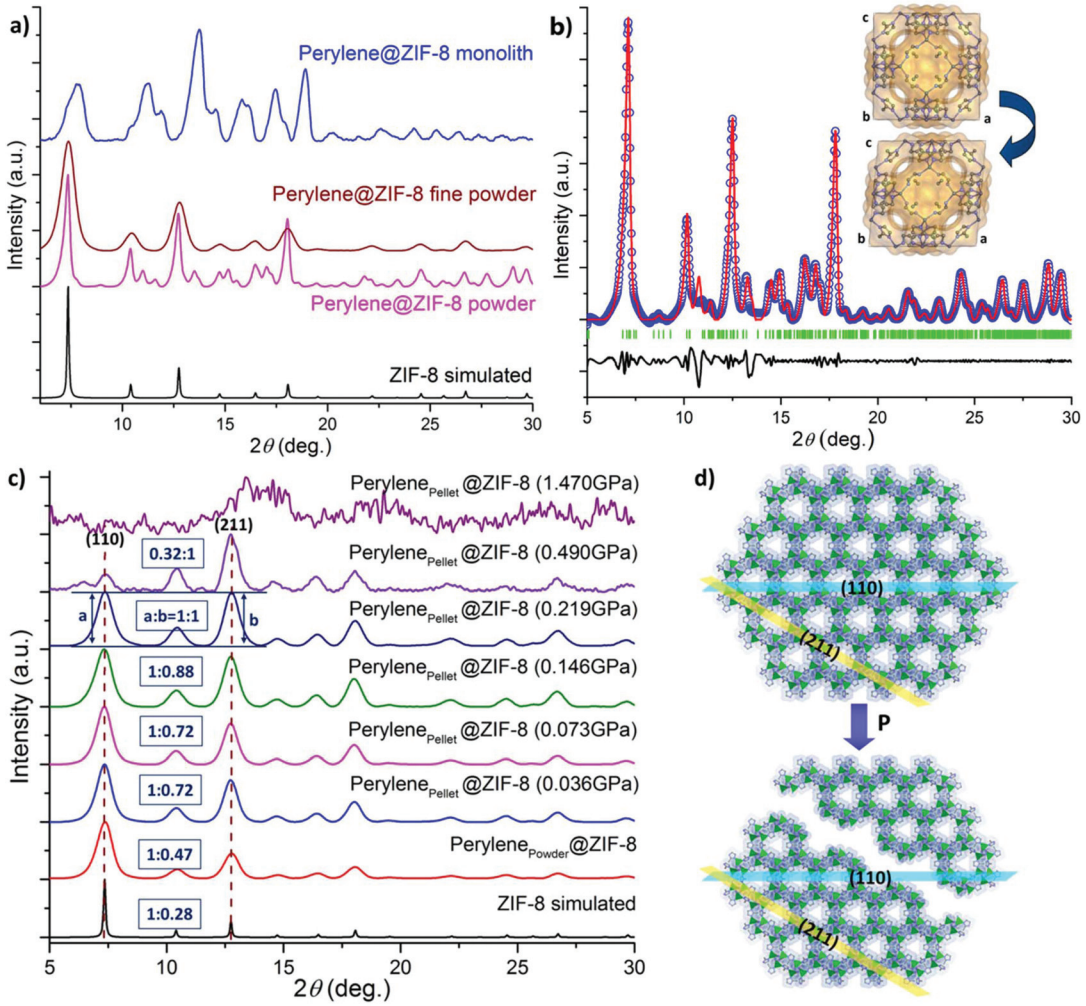

Fig. 6 (a) Comparison of the XRD patterns of the monolithic, powder (5 min grinding in a mortar), and fine powder forms (20 min grinding) of Perylene@ZIF-8. (b) Pawley structural refinement (R_{wp} = 8.2%) of an X-ray diffraction pattern of the powder sample of Perylene@ZIF-8. Symbols used: the blue circles are the experimental data; the red line is the calculated pattern; the green bars represent the observed Bragg reflections; the bottom black lines are the structural refinement residuals. The inset shows the structural distortions of ZIF-8 viewed along the *b*-axis. (c) Systematic XRD study to monitor the changes in the relative peak intensities of the {110}- and {211}-oriented crystallographic planes upon the compression of the fine powdered Perylene@ZIF-8 sample using different pressures. (d) Proposed structural fracture mechanism endorsed by XRD data, suggesting the cleavage of Perylene@ZIF-8 nanoplates across the {211} plane due to the shearing deformation attributed to compressive stress, eventually causing amorphization of the compound at around 1.5 GPa.

the emission spectra of the samples ground for 5 min (powder) *vs.* the samples ground for 20 min (fine powder), but no changes were detected. To further investigate the ability of the reconstituted Perylene@ZIF-8 fine powder to exhibit a red shift beyond 502 nm, we systematically prepared a series of pellets using higher pressures and monitored their structural evolution by XRD (Fig. 6c) and emission spectroscopy. We found that the emission of the reconstituted pellets remains unchanged at 502 nm (Fig. S6†) for all pellets prepared from a stress as low as 0.036 GPa to a maximum stress of 1.47 GPa. The abovementioned results support the notion that the aggregated nanoplates in the monolithic form are very tightly packed together (yielding emission at 510 nm), which cannot be regained in the reconstituted powder pellets (less dense, thus, lower emission at 502 nm).

Detailed analysis of the relative peak intensities from XRD data of different pellets prepared with ascending pressures can give us a deeper insight into the structural changes of the material. Fig. 6c shows a decreasing trend in the intensity of the (110) plane, accompanied by a gradual increase in the intensity of the (211) plane. The ratios of the changing relative peak intensities of the (110) : (211) planes are summarized in Fig. 6c, where the initial ratio rises from 1 : 0.47 for a ground fine powder sample to 1 : 1 for the pellet pressurized at 0.219 GPa. Then, on more than doubling the pelleting pressure to 0.49 GPa, we obtained the peak ratio of 0.32 : 1 alongside the appearance of the extra diffraction peaks. Eventually at a significantly higher pressure of 1.47 GPa, the disappearance of all of the Bragg peaks associated with ZIF-8 were observed because of the framework amorphization.[53] Fig. 6d illustrates

the proposed fracture mode of ZIF-8 that can account for such a phenomenon, in which the cleavage planes orient along the {211} facet, ruptured by the shear stresses. In fact, this failure mechanism is reminiscent to that reported for ZIF-8 subjected to a high-rate impact mechanical deformation, which also led to the formation of the preferred {211}-oriented planes.[54]

Significantly, all of the pellets described above show reversible mechanochromic behavior. Surprisingly, the amorphized sample prepared at 1.47 GPa remains mechanochromic by retaining its emission at 502 nm. This finding suggests that the spatial confinement of Perylene within the pores of ZIF-8 remains effective despite the host framework losing its long-range periodicity *via* amorphization. Finally, thermogravimetric analysis (TGA) of the Perylene@ZIF-8 powder (Fig. S6†) indicated that the thermal stability of the monolithic form is higher than that of its powdered form by about 200 °C. This finding supports a denser arrangement of nanoplates in the monolithic form possessing a greater thermal stability than its fine powder form.

3. Conclusions

In summary, we shed new light on the use of orderly-arranged voids conferred by the MOF compounds acting as a 3-D nanoscale scaffolding to spatially isolate the emissive guest molecules for accomplishing a unique "solution-like" luminescent behavior. In our material design, we employed an optically-inactive MOF host (a sodalite cage of ZIF-8) for the spatial confinement of a bulky polycyclic fluorophore guest (Perylene), resulting in a novel Guest@MOF system—Perylene@ZIF-8—with switchable emission properties (442 ⇌ 502 nm) when it is subjected to a reversible mechanical stress or hydrostatic pressure. We harnessed the high-concentration reaction (HCR) synthetic strategy for morphology control, yielding the nanoplates of an inherently 3-D ZIF-8 structure co-assembled with the Perylene guests. Remarkably, such nanoscale 2-D configuration permits a facile aggregation and separation of Perylene@ZIF-8 nanoplates under stress (of tens of MPa), which is responsible for the reversible mechanochromic luminescence phenomenon recorded in our study. Furthermore, we discovered that the structural transition from a crystalline to amorphous phase could retain its mechanochromic properties, thus opening up an exciting route for fabricating the functional amorphous materials constituting photonic Guest@MOF nanocomposites. Collectively, our new findings and innovative approach towards mechanochromism will be valuable in expanding the frontier of MOF science, particularly in the pursuit of next-generation host–guest nanomaterials exhibiting the tunable optoelectronic and sensing properties.

Conflicts of interest

There are no conflicts to declare.

Acknowledgements

This research was funded by the Samsung Advanced Institute of Technology (SAIT) GRO and the Engineering and Physical Sciences Research Council, EPSRC RCUK (EP/N014960/1 and EP/K031503/1). We are very grateful to Dr Gavin Stenning and Dr Marek Jura at the R53 Materials Characterisation Lab in the ISIS Rutherford Appleton Laboratory for the provision of X-ray diffraction facilities. We thank the Research Complex at Harwell (RCaH), Oxfordshire, for allowing access to the TEM and UV-Vis facilities.

References

1 J. Choi, H. Zhang and J. H. Choi, *ACS Nano*, 2016, **10**, 1671–1680.
2 Y. S. Zhao, H. B. Fu, A. D. Peng, Y. Ma, D. B. Xiao and J. N. Yao, *Adv. Mater.*, 2008, **20**, 2859–2876.
3 H. Xu, R. Chen, Q. Sun, W. Lai, Q. Su, W. Huang and X. Liu, *Chem. Soc. Rev.*, 2014, **43**, 3259–3302.
4 E. A. Dolgopolova and N. B. Shustova, *MRS Bull.*, 2016, **41**, 890–895.
5 M. J. Serpe, Y. Kang and Q. M. Zhang, *Photonic Materials for Sensing, Biosensing and Display Devices Preface*, Springer, 2016.
6 I. Stassen, N. Burtch, A. Talin, P. Falcaro, M. Allendorf and R. Ameloot, *Chem. Soc. Rev.*, 2017, **46**, 3185–3241.
7 J. T. Suri, D. B. Cordes, F. E. Cappuccio, R. A. Wessling and B. Singaram, *Angew. Chem., Int. Ed.*, 2003, **42**, 5857–5859.
8 M. D. Ward, *Chem. Soc. Rev.*, 1997, **26**, 365–375.
9 T. Aida, E. W. Meijer and S. I. Stupp, *Science*, 2012, **335**, 813–817.
10 I. Yildiz, M. Tomasulo and F. M. Raymo, *Proc. Natl. Acad. Sci. U. S. A.*, 2006, **103**, 11457–11460.
11 K. Ariga, T. Mori and J. P. Hill, *Adv. Mater.*, 2012, **24**, 158–176.
12 X. Hou, C. Ke, C. J. Bruns, P. R. McGonigal, R. B. Pettman and J. F. Stoddart, *Nat. Commun.*, 2015, **6**, 6884–6893.
13 Y. Wang, X. Tan, Y. M. Zhang, S. Zhu, I. Zhang, B. Yu, K. Wang, B. Yang, M. Li, B. Zou and S. X. Zhang, *J. Am. Chem. Soc.*, 2015, **137**, 931–939.
14 E. Boldyreva, *Chem. Soc. Rev.*, 2013, **42**, 7719–7738.
15 G. Kaupp, *CrystEngComm*, 2009, **11**, 388–403.
16 Z. K. He, L. Q. Zhang, J. Mei, T. Zhang, J. W. Y. Lam, Z. G. Shuai, Y. Q. Dong and B. Z. Tang, *Chem. Mater.*, 2015, **27**, 6601–6607.
17 Z. Chen, J. Zhang, M. Song, J. Yin, G. A. Yu and S. H. Liu, *Chem. Commun.*, 2015, **51**, 326–329.
18 R. Misra, T. Jadhav, B. Dhokale and S. M. Mobin, *Chem. Commun.*, 2014, **50**, 9076–9078.
19 Q. Benito, X. F. Le Goff, S. Maron, A. Fargues, A. Garcia, C. Martineau, F. Taulelle, S. Kahlal, T. Gacoin, J. P. Boilot and S. Perruchas, *J. Am. Chem. Soc.*, 2014, **136**, 11311–11320.

20 M. D. Allendorf, R. Medishetty and R. A. Fischer, *MRS Bull.*, 2016, **41**, 865–869.
21 (*a*) A. K. Chaudhari, H. J. Kim, I. Han and J. C. Tan, *Adv. Mater.*, 2017, **29**, 1701463; (*b*) A. K. Chaudhari and J. C. Tan, *Chem. Commun.*, 2017, **53**, 8491–8626.
22 A. K. Chaudhari, M. R. Ryder and J. C. Tan, *Nanoscale*, 2016, **8**, 6851–6859.
23 H. Mieno, R. Kabe, N. Notsuka, M. D. Allendorf and C. Adachi, *Adv. Opt. Mater.*, 2016, **4**, 1015–1021.
24 J. C. Tan and B. Civalleri, *CrystEngComm*, 2015, **17**, 197–198.
25 S. Kitagawa, R. Kitaura and S. Noro, *Angew. Chem., Int. Ed.*, 2004, **43**, 2334–2375.
26 B. F. Hoskins and R. Robson, *J. Am. Chem. Soc.*, 1989, **111**, 5962–5964.
27 S. Subramanian and M. J. Zaworotko, *Angew. Chem., Int. Ed. Engl.*, 1995, **34**, 2127–2129.
28 O. M. Yaghi, H. L. Li, C. Davis, D. Richardson and T. L. Groy, *Acc. Chem. Res.*, 1998, **31**, 474–484.
29 M. R. Ryder and J. C. Tan, *Mater. Sci. Technol.*, 2014, **30**, 1598–1612.
30 K. S. Park, Z. Ni, A. P. Cote, J. Y. Choi, R. Huang, F. J. Uribe-Romo, H. K. Chae, M. O'Keeffe and O. M. Yaghi, *Proc. Natl. Acad. Sci. U. S. A.*, 2006, **103**, 10186–10191.
31 M. R. Ryder, B. Civalleri, T. D. Bennett, S. Henke, S. Rudic, G. Cinque, F. Fernandez-Alonso and J. C. Tan, *Phys. Rev. Lett.*, 2014, **113**, 215502.
32 B. C. Tzeng, T. Y. Chang and H. S. Sheu, *Chem. – Eur. J.*, 2010, **16**, 9990–9993.
33 T. Wen, X. P. Zhou, D. X. Zhang and D. Li, *Chem. – Eur. J.*, 2014, **20**, 644–648.
34 J. K. Sun, C. Chen, L. X. Cai, C. X. Ren, B. Tan and J. Zhang, *Chem. Commun.*, 2014, **50**, 15956–15959.
35 M. S. Deshmukh, A. Yadav, R. Pant and R. Boomishankar, *Inorg. Chem.*, 2015, **54**, 1337–1345.
36 Q. Zhang, J. Su, D. Feng, Z. Wei, X. Zou and H. C. Zhou, *J. Am. Chem. Soc.*, 2015, **137**, 10064–10067.
37 J. C. Tan, T. D. Bennett and A. K. Cheetham, *Proc. Natl. Acad. Sci. U. S. A.*, 2010, **107**, 9938–9943.
38 D. Esken, S. Turner, C. Wiktor, S. B. Kalidindi, G. Van Tendeloo and R. A. Fischer, *J. Am. Chem. Soc.*, 2011, **133**, 16370–16373.
39 N. Liedana, A. Galve, C. Rubio, C. Tellez and J. Coronas, *ACS Appl. Mater. Interfaces*, 2012, **4**, 5016–5021.
40 G. Lu, S. Li, Z. Guo, O. K. Farha, B. G. Hauser, X. Qi, Y. Wang, X. Wang, S. Han, X. Liu, J. S. DuChene, H. Zhang, Q. Zhang, X. Chen, J. Ma, S. C. Loo, W. D. Wei, Y. Yang, J. T. Hupp and F. Huo, *Nat. Chem.*, 2012, **4**, 310–316.
41 B. P. Biswal, D. B. Shinde, V. K. Pillai and R. Banerjee, *Nanoscale*, 2013, **5**, 10556–10561.
42 J. Zhuang, C. H. Kuo, L. Y. Chou, D. Y. Liu, E. Weerapana and C. K. Tsung, *ACS Nano*, 2014, **8**, 2812–2819.
43 X. Lin, G. Gao, L. Zheng, Y. Chi and G. Chen, *Anal. Chem.*, 2014, **86**, 1223–1228.
44 F. Lyu, Y. Zhang, R. N. Zare, J. Ge and Z. Liu, *Nano Lett.*, 2014, **14**, 5761–5765.
45 Y. Song, D. Hu, F. Liu, S. Chen and L. Wang, *Analyst*, 2015, **140**, 623–629.
46 J. C. Tan, B. Civalleri, C. C. Lin, L. Valenzano, R. Galvelis, P. F. Chen, T. D. Bennett, C. Mellot-Draznieks, C. M. Zicovich-Wilson and A. K. Cheetham, *Phys. Rev. Lett.*, 2012, **108**, 095502.
47 A. K. Chaudhari, I. Han and J. C. Tan, *Adv. Mater.*, 2015, **27**, 4438–4446.
48 J. Ferguson, *J. Chem. Phys.*, 1966, **44**, 2677–2683.
49 M. D. Allendorf, C. A. Bauer, R. K. Bhakta and R. J. Houk, *Chem. Soc. Rev.*, 2009, **38**, 1330–1352.
50 F. C. Spano and C. Silva, *Annu. Rev. Phys. Chem.*, 2014, **65**, 477–500.
51 E. Holder, N. Tessler and A. L. Rogach, *J. Mater. Chem.*, 2008, **18**, 1064–1078.
52 Q. Zhou and T. M. Swager, *J. Am. Chem. Soc.*, 1995, **117**, 12593–12602.
53 S. Cao, T. D. Bennett, D. A. Keen, A. L. Goodwin and A. K. Cheetham, *Chem. Commun.*, 2012, **48**, 7805–7807.
54 D. Y. Kim, B. N. Joshi, J. G. Lee, J. H. Lee, J. S. Lee, Y. K. Hwang, J. S. Chang, S. Al-Deyab, J. C. Tan and S. S. Yoon, *Chem. Eng. J.*, 2016, **295**, 49–56.

